

www.acsami.org Research Article

Elucidating Structure—Composition—Property Relationships of Ni-Based Prussian Blue Analogues for Electrochemical Seawater Desalination

Margaret A. Lumley, Do-Hwan Nam, and Kyoung-Shin Choi*



Cite This: ACS Appl. Mater. Interfaces 2020, 12, 36014-36025



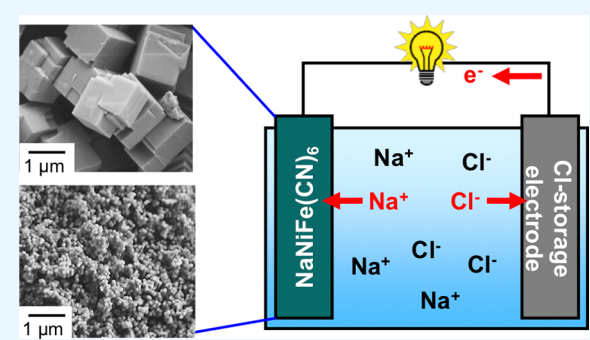
ACCESS

III Metrics & More



Supporting Information

ABSTRACT: Nickel hexacyanoferrate (NiHCF), a type of Prussian blue analogue (PBA), has recently emerged as one of the most promising Nastorage electrodes for use in electrochemical desalination. Previous studies have revealed that NiHCF can be prepared with both cubic and rhombohedral symmetries depending on the oxidation state of Fe (Fe^{II} vs Fe^{III}) and the related A-site occupancy. However, our understanding of the effects of the lattice-type of the as-prepared samples on their electrochemical performances, structural transitions that occur during sodiation/desodiation, cyclability, and rate capabilities is presently lacking. Additionally, the optimum structural and compositional features required to prepare high-performing NiHCF electrodes have not yet been clearly established. In this work, we report the synthesis of two sets of cubic and



rhombohedral NiHCF samples with different particle sizes, crystallinities, and compositions. Using these samples, we systematically elucidated the structure—composition—property relationships of NiHCF to develop rational design principles to prepare high-performing PBAs. Our results show that high crystallinity, a low number of $Fe(CN)_6$ vacancies, and a large unit cell size to allow for consistent structural changes during cycling are critical factors to produce NiHCF with a high capacity, good cycling stability, and good rate capabilities, and these factors are considerably affected by the synthesis conditions. One of the samples prepared in this study with optimum structural features demonstrates the best performance and stability among any PBA electrode tested in neutral saline solutions to date.

KEYWORDS: nickel hexacyanoferrate, Prussian blue analogue, Na-storage electrode, electrochemical desalination, desalination battery, Na-ion battery

1. INTRODUCTION

Steady growth in human population and rapid industrial development have led to greater demands for water production for agriculture, energy generation, and human consumption, and global water demand is expected to increase by 70% from 2016 to 2050 if global warming continues at the current rate. As more than 97% of Earth's water exists as ocean water, desalination of seawater is considered the most viable option to meet the increasing demand for freshwater. 1-6 Recently, various new electrochemical desalination strategies have been explored to complement traditional desalination methods such as distillation and reverse osmosis that are based on physical processes.^{7–26} Many of these electrochemical desalination methods involve the use of Na-storage electrodes that can store Na⁺ in the bulk of the electrode material via electrochemical reactions. Pecause of the development of Na-ion batteries, numerous possible Na-storage materials have already been identified. 22,23,27 The most representative electrochemical desalination methods based on the use of Na-storage electrodes are illustrated in Figure 1.

The first method is a desalination battery where a Nastorage electrode is combined with a Cl-storage electrode that stores Cl⁻ in the bulk of the electrode (Figure 1a).^{7–11,13} During the desalination step, the Na-storage electrode and Cl-storage electrode will become saturated with Na⁺ and Cl⁻, respectively. To regenerate the electrodes, they can be moved to a separate cell to release Na⁺ and Cl⁻ in a salination step, generating brine and enabling the electrodes to be recovered and used for subsequent desalination cycles. The second method combines two Na-storage electrodes that are separated by an anion exchange membrane (AEM) (Figure 1b).^{16–18} The Na-storage electrode in the cathode compartment removes Na⁺ from the catholyte (sodiation), and the Na-

Received: May 2, 2020 Accepted: July 16, 2020 Published: August 3, 2020





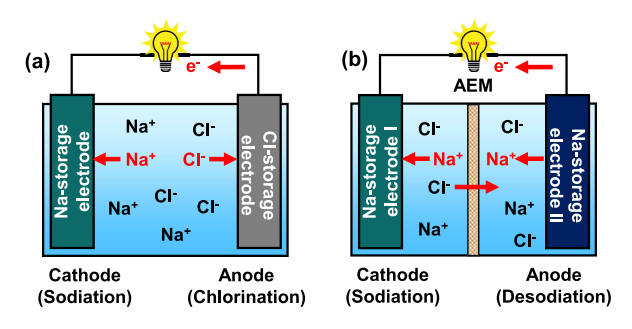


Figure 1. Electrochemical desalination cells containing Na-storage electrodes: (a) a desalination battery where a Na-storage electrode is paired with a Cl-storage electrode and (b) a rocking chair desalination battery where two different Na-storage electrodes are separated by an anion exchange membrane (AEM). For simplicity, only the desalination step is shown here. In this example, the cathode potential is more positive than the anode potential during desalination, equivalent to discharging.

storage electrode in the anode compartment releases Na⁺ into the anolyte (desodiation). To maintain charge neutrality in both compartments, Cl⁻ will move from the catholyte to the anolyte through the AEM to achieve desalination in the catholyte and produce brine in the anolyte. Once the Nastorage electrode in the cathode compartment is saturated with Na⁺ and the Na-storage electrode in the anode compartment has released all Na⁺, the electrodes can simply be swapped to continue desalination. In this type of desalination cell, the two Na-storage electrodes can be identical or different. When the two Na-storage electrodes are identical, the cell is called a symmetric Na-ion desalination cell. ^{17,18} When the two Nastorage electrodes are different, the cell is called a rocking chair desalination battery, depicted in Figure 1b. ¹⁶

For practical seawater desalination applications, the Nastorage electrodes must efficiently store and release Na⁺ in seawater with long-term stability. One of the most promising classes of Na-storage electrodes for desalination applications is Prussian blue analogues (PBAs)^{13,16–21} with the nominal formula A_x MFe(CN)₆·nH₂O (A is an alkali metal ion, and M is a divalent transition metal ion, $1 \le x \le 2$) (Figure 2).

In this structure, M and Fe ions occupy alternating corner sites of cubes and the CN ligands are located along the edges of the cubes. ^{23,28-31} The M ions are octahedrally coordinated to the nitrogen ends of CN ligands, and the Fe ions are

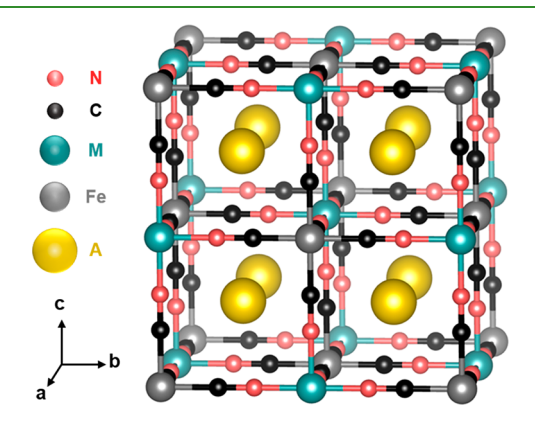


Figure 2. Prussian blue analogue (PBA) unit cell. The fully reduced form of the PBA is shown here, with the general formula $A_2MFe^{II}(CN)_6$ (A = alkali metal ion; M = divalent transition metal ion).

octahedrally coordinated to the carbon ends of CN ligands to form a framework of -NC-Fe-CN-M-NC- linear linkages. The A ions occupy the body center of the cube, and the site occupancy is directly related to the oxidation state of Fe. During desalination, the A-site will be occupied by Na⁺. When all Fe ions exist as Fe^{III}, the maximum amount of Na⁺ per empirical formula unit is 1. This is equivalent to having Na⁺ located in half of the body center sites. When all Fe ions exist as Fe^{II}, the maximum amount of Na⁺ per empirical formula unit increases to 2, equivalent to having Na⁺ located in all of the body center sites. The electrochemical reaction that induces Na-storage and release is shown in eq 1.

$$NaM^{II}Fe^{III}(CN)_{6} + xNa^{+} + xe^{-} \rightleftharpoons Na_{1+x}M^{II}Fe_{x}^{II}Fe_{1-x}^{III}(CN)_{6} \quad (0 \le x \le 1)$$
 (1)

PBAs can be easily synthesized from aqueous precipitation reactions and are inexpensive to produce, ³² which makes them promising candidates for large-scale desalination. Additionally, PBAs have demonstrated exceptional stability in electrolytes used for Na-ion battery applications. ^{28,33–39} However, to date, PBAs tested for desalination applications in neutral aqueous media have commonly shown some capacity fading within 100 cycles, ^{13,16,17,21} even when an electrolyte containing a low salt concentration (i.e., 50 mM NaCl) has been used. ¹⁷ This warrants considerable and systematic efforts to understand and improve the performance of PBAs for desalination applications.

One important consideration for choosing the type of PBA to use for desalination is its sodiation/desodiation potential relative to the water reduction and oxidation potentials in neutral aqueous electrolytes. In this context, nickel hexacyanoferrate (NiHCF) is particularly attractive, as its operating window lies between the water reduction and oxidation potentials in neutral aqueous electrolytes. Therefore, sodiation and desodiation will occur without interference from water reduction or oxidation. However, to date, there have been only a few reports on the performance of NiHCF in neutral aqueous electrolytes containing Cl^{-13,16-21,40} and more systematic studies are necessary to evaluate NiHCF as a possible Na-storage electrode for desalination.

Examining previous reports on the performance of NiHCF for Na-ion battery applications revealed a few interesting yet ill-understood features of NiHCF. First, NiHCF can be prepared with both cubic and rhombohedral symmetries and the rhombohedral phase is generally reported to exhibit higher capacities and better rate capabilities than the cubic phase. 35,41 However, we note that the cubic and rhombohedral NiHCF samples compared in these studies are often prepared with different morphologies (size and shape of particles) or crystallinities (the quality of the cubic NiHCF sample is usually worse than that of the corresponding rhombohedral sample). Thus, the features that are required to fabricate highperforming NiHCF electrodes remain unclear. For example, if cubic and rhombohedral NiHCF are prepared with the same morphology, particle size, and crystallinity, will rhombohedral NiHCF still be superior? Or is it not the lattice-type but the morphology, particle size, and crystallinity that govern the performance of NiHCF?

Second, the lattice-type of NiHCF is closely related to the oxidation state of Fe in the as-prepared sample. When NiHCF is prepared with a high amount of Fe^{III} and therefore contains a low amount of Na⁺, it has a cubic lattice. When NiHCF is prepared with a high amount of Fe^{II} and therefore contains a

high amount of Na⁺, it has a rhombohedral lattice. ^{35,41} It has also been reported previously that during desodiation (oxidation of Fe^{II} to Fe^{III}), rhombohedral NiHCF will undergo a transition to cubic NiHCF. ^{35,42} This observation raised a few important questions about the relationship between the lattice-type, redox chemistry, and sodiation/desodiation performance of NiHCF. For example, will NiHCF always undergo the same structural transformation during sodiation and desodiation, regardless of the lattice-type of the as-prepared sample (i.e., cubic vs rhombohedral)? If so, why is the initial lattice-type important and why does it affect the performance of NiHCF?

The study reported here was designed to answer these critical questions to increase our general understanding of NiHCF and prepare high-performing NiHCF electrodes for desalination applications. To achieve this goal, we synthesized two sets of cubic and rhombohedral NiHCF samples with comparable morphologies and crystallinities. The first set was prepared at room temperature and had relatively low crystallinity, and the second set was prepared at an elevated temperature and was highly crystalline. The sodiation and desodiation performances of the resulting samples were investigated in 0.6 M NaCl solutions to mimic the salinity of seawater. By systematically analyzing their structures, compositions, performances, stabilities, and rate capabilities as well as the phase transformations that occur during the sodiation and desodiation reactions, we offer new insights to understand the key factors that affect the performance of NiHCF as a Nastorage electrode. To the best of our knowledge, one of the samples prepared in this study with optimum structural features demonstrates the best performance and stability among any PBA electrode tested in neutral saline solutions to date. We believe that the new insights provided in this study are important not only for desalination applications but also for the use of PBAs as Na-storage electrodes in Na-ion batteries.

2. EXPERIMENTAL SECTION

Materials. NiCl₂·6H₂O (98%, Alfa Aesar), Na₃C₆H₅O₇·2H₂O (≥98%, Mallinckrodt), Na₄Fe(CN)₆·10H₂O (≥99%, Sigma-Aldrich), K₃Fe(CN)₆ (99.7%, Fisher), polytetrafluoroethylene (PTFE) (60 wt % dispersion in H₂O, Sigma-Aldrich), Super C65 (TimCal), colloidal graphite (isopropanol, Ted Pella, Inc.), NaCl (99%, Macron), and EtOH (200 proof, Decon Labs Inc.) were used without further purification. Deionized water (Barnstead E-pure water purification system, resistivity of >18 MΩ·cm) was used to prepare all solutions.

Synthesis of Rhombohedral NiHCF (r-NiHCF). Rhombohedral NiHCF (r-NiHCF) was synthesized by modifying a co-precipitation method reported in a previous study. First, 0.10 M NiCl₂ and 0.70 M Na₃C₆H₅O₇ (Na-citrate) were dissolved in 150 mL of water at room temperature (RT). Na-citrate was used as a complexing agent to control the rate of precipitation. A 150 mL solution containing 0.10 M Na₄Fe(CN)₆ was then added to the NiCl₂/Na-citrate solution under vigorous stirring. The reaction was vigorously stirred at RT for 5 h, and a pale green precipitate became evident as the reaction progressed. The solution was then aged at RT for 20 h. The resulting precipitate was centrifuged at 5000 rpm and washed alternately with water and ethanol until the washing solution was clear. Finally, the precipitate was dried at 70 °C for 24 h in a vacuum furnace held at a pressure of ~13.6 psi. The resulting powder was pale green in color.

The synthesis of r-NiHCF was also performed at 90 °C to improve the crystallinity of r-NiHCF. Briefly, 0.10 M NiCl₂ and 0.70 M Nacitrate were dissolved in 150 mL of water and the solution was heated to 90 °C. A 150 mL solution containing 0.10 M Na₄Fe(CN)₆ was also heated to 90 °C and was then added to the NiCl₂/Na-citrate solution under vigorous stirring. The reaction was vigorously stirred at 90 °C for 5 h, and a pale green precipitate became evident as the reaction progressed. The solution was then aged at RT for 20 h and was

washed and dried following the same procedure that was used for the RT sample. The resulting powder was pale green in color.

Synthesis of Cubic NiHCF (c-NiHCF). Cubic NiHCF (c-NiHCF) was synthesized by modifying the procedure described above for r-NiHCF. First, K₃Fe(CN)₆ was used as the Fe-precursor rather than Na₄Fe(CN)₆. Similar modifications for the synthesis of c-NiHCF have also been reported by other groups. The amount of Na-citrate used for the synthesis was also reduced from 0.70 to 0.175 M to facilitate the precipitation of c-NiHCF (when 0.70 M Na-citrate was used, only a very small amount of product formed on the time scale of the reaction). All other reaction conditions were the same as for r-NiHCF described above.

The RT reaction was carried out by dissolving 0.10 M NiCl₂ and 0.175 M Na-citrate in 150 mL of water at RT. A 150 mL solution containing 0.10 M $\rm K_3Fe(CN)_6$ was then added to the NiCl₂/Na-citrate solution under vigorous stirring. The reaction was vigorously stirred at RT for 5 h, and an orange precipitate became evident as the reaction progressed. The solution was then aged at RT for 20 h. The resulting precipitate was centrifuged at 5000 rpm and washed alternately with water and ethanol until the washing solution was clear. Finally, the precipitate was dried at 70 $^{\circ}$ C for 24 h in a vacuum furnace held at a pressure of $\sim \! 13.6$ psi. The resulting powder was orange in color.

The synthesis of c-NiHCF was also performed at 70 °C to improve the crystallinity of the compound. When a higher temperature of 90 °C was used for the preparation of c-NiHCF, cracks in the NiHCF crystals were evident by scanning electron microscopy (SEM). Thus, a maximum synthesis temperature of 70 °C was chosen for c-NiHCF. Briefly, 0.10 M NiCl₂ and 0.175 M Na-citrate were dissolved in 150 mL of water and the solution was heated to 70 °C. A 150 mL solution containing 0.10 M K₃Fe(CN)₆ was also heated to 70 °C and was then added to the NiCl₂/Na-citrate solution under vigorous stirring. The reaction was vigorously stirred at 70 °C for 5 h, and an orange precipitate became evident as the reaction progressed. The reaction was then aged at RT for 20 h and was washed and dried following the same procedure outlined above for the RT sample. The resulting powder was orange in color.

Preparation of NiHCF Electrodes. To prepare NiHCF electrodes, the as-prepared NiHCF powder was first ground with a mortar and pestle into a fine powder. The resulting NiHCF powder (0.25 g) was then ground in a mortar and pestle with Super C65 (0.083 g) and a PTFE binder $(100 \, \mu\text{L})$ with a ratio of 60:20:20 by mass using water as the solvent. The paste that formed was kneaded and rolled into a sheet using a roll-press to prepare sheet-type electrodes with a thickness of ~100 μ m. The sheets were dried at 45 °C for 3 h to remove any residual water. An electrode with an area of 1 cm² was punched from the sheet and attached onto a graphite current collector using colloidal graphite paste. The average mass of NiHCF in the electrodes was ~0.007 g/cm².

Characterization. X-ray diffraction (XRD) patterns were collected on a Bruker D8 diffractometer with Ni-filtered Cu $K\alpha$ radiation ($\lambda=1.5418$ Å). The morphology of the NiHCF powders was examined using a LEO SupraS5 VP scanning electron microscope (SEM) operated at an accelerating voltage of 2 kV. Energy dispersive X-ray spectroscopy (EDS) was performed using the same SEM equipped with an EDS (Noran System Seven, Thermo Fisher) at an accelerating voltage of 12 kV. The water content of each sample was investigated using thermogravimetric analysis (TGA) with a TA Instruments Q500 TGA. The samples were heated from 24 to 250 °C using a ramp rate of 5 °C/min.

Electrochemical Testing. An undivided three-electrode cell was used for all electrochemical tests. The performances of r-NiHCF and c-NiHCF were examined using 0.6 M NaCl as the electrolyte to mimic the salinity of seawater. The reference electrode (RE) was a double junction Ag/AgCl RE (4 M KCl). NiHCF was used as both the working electrode (WE) and counter electrode (CE) for all electrochemical tests. The WE and CE contained similar masses of active material, and both had an area of 1 cm². Prior to electrochemical tests the WE was oxidized (desodiated) by applying a potential of 0.75 V vs Ag/AgCl for 20 min and the CE was reduced

(sodiated) by applying a potential of 0.1 V vs Ag/AgCl for 20 min. Previously, we reported half-cell tests of copper HCF (CuHCF) in 0.6 M NaCl using a Pt CE. ¹³ However, during cycling tests we observed an increase in the pH of the solution due to water reduction occurring on the Pt CE. The increase in pH combined with a high concentration of Cl⁻ in the electrolyte resulted in degradation of the CuHCF WE. Thus, to prevent any possible effects caused by an increase in pH, a NiHCF CE was used in these studies.

The volume of each electrolyte was ~140 mL, and galvanostatic cycling was used for all tests. Galvanostatic sodiation/desodiation tests were performed with cutoff potentials of 0 and 0.85 V vs Ag/AgCl for sodiation and desodiation, respectively, at a current density of ± 1 mA cm⁻² (± 145 mA g⁻¹). This corresponds to a rate of ~2.5C if we assume that 1C rate for NiHCF is 60 mA g⁻¹. Sequence color voltammograms (CVs) were obtained in the same three-electrode setup using a scan rate of 2 mV s⁻¹. All NiHCF WEs were desodiated prior to performing CVs. The rate capabilities of the various NiHCF electrodes were investigated by applying current densities of ± 1 mA cm⁻² (145 mA g⁻¹ or ~2.5C), 2 mA cm⁻² (290 mA g⁻¹ or ~5C), 4 mA cm⁻² (580 mA g⁻¹ or ~10C), and 8 mA cm⁻² (1160 mA g⁻¹ or ~20C) in the same three-electrode setup.

3. RESULTS AND DISCUSSION

Synthesis and Characterization of Cubic (c-) and Rhombohedral (r-) NiHCF. In order to investigate the effect of lattice-type, morphology, and crystallinity of NiHCF on its desalination performance, two sets of cubic NiHCF (c-NiHCF) and rhombohedral NiHCF (r-NiHCF) samples were prepared via aqueous precipitation reactions, and the samples in each set had comparable morphologies. The first set of samples was prepared at room temperature (RT), and these samples will be denoted as c-NiHCF-RT and r-NiHCF-RT. The key parameter that affects the lattice-type of NiHCF (cubic vs rhombohedral) is the oxidation state of Fe in the structure. 35,41 To prepare c-NiHCF, K₃Fe(CN)₆ was used as the precursor, and to prepare r-NiHCF, Na₄Fe(CN)₆ was used as the precursor. When an Fe^{III} precursor is used, an oxidized form of NiHCF forms with a lower Na⁺ content and crystallizes with cubic symmetry. When an Fe^{II} precursor is used and it is maintained as Fe^{II} during the synthesis, a more reduced form of NiHCF forms with a greater Na+ content and crystallizes with rhombohedral symmetry.

The morphologies of c-NiHCF-RT and r-NiHCF-RT were first investigated by SEM (Figure 3a,b), which revealed that the two samples have comparable particle sizes (average diameter of ~200 nm). However, high magnification SEM images show that the c-NiHCF-RT particles have a more welldefined cubic shape while the r-NiHCF-RT particles are more spherical in shape. The formation of the cubic and rhombohedral phases was confirmed by XRD. All peaks in the XRD pattern of c-NiHCF-RT can be indexed with the cubic PBA structure (Figure 4a). The formation of the rhombohedral phase can be confirmed through the observation of splitting of the peaks present in the cubic NiHCF XRD pattern. Most notably, the 220, 420, 440, and 620 peaks of c-NiHCF-RT appear as doublets in the XRD pattern of r-NiHCF-RT (Figure 4b). 16,35,41,42 We note that the hkl indices shown for the rhombohedral samples in Figure 4b are based on the use of a rhombohedral cell rather than an R-centered hexagonal cell. As the cubic and rhombohedral cells have the same crystallographic axes, choosing to index peaks in this way allows us to easily compare the peak positions and peak splitting of cubic and rhombohedral samples. Examining the full width at half-maximum (FWHM) of the (200) peak reveals that c-NiHCF-RT is more crystalline than r-NiHCF-RT

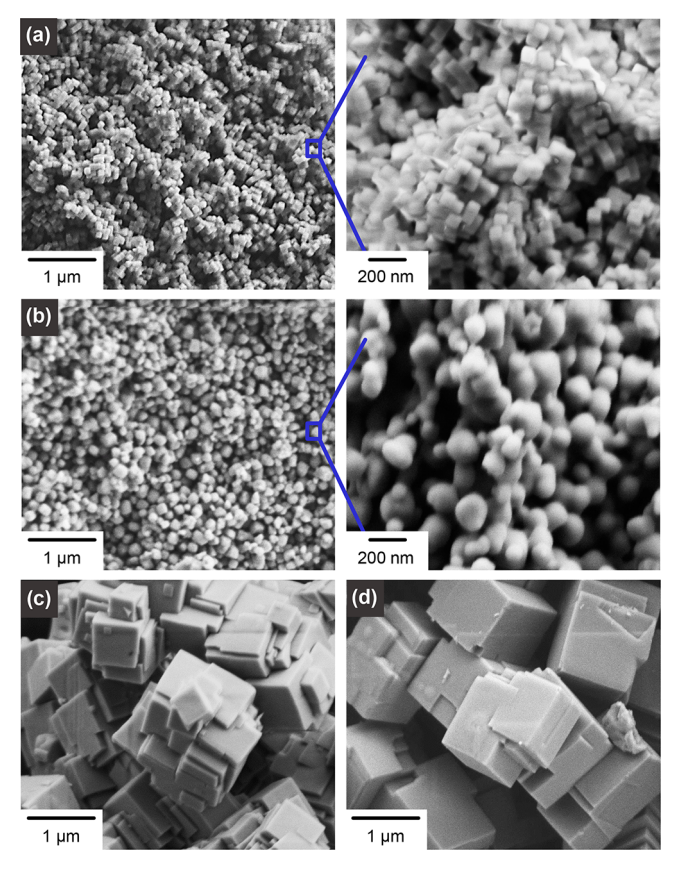


Figure 3. SEM images of (a) c-NiHCF-RT, (b) r-NiHCF-RT, (c) c-NiHCF-70°C, and (d) r-NiHCF-90°C. Higher magnification images are also shown for (a) c-NiHCF-RT and (b) r-NiHCF-RT.

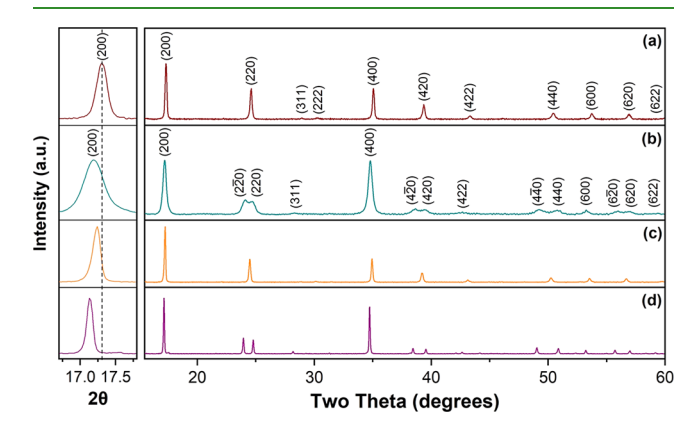


Figure 4. XRD patterns of (a) c-NiHCF-RT, (b) r-NiHCF-RT, (c) c-NiHCF-70 $^{\circ}$ C, and (d) r-NiHCF-90 $^{\circ}$ C. The left panel shows a close-up image of the (200) peak of each sample.

(Figure 4a,b, left panels), which agrees well with the SEM images.

The second set of c-NiHCF and r-NiHCF samples was prepared at an elevated temperature to improve the sample crystallinity. The synthesis of c-NiHCF was performed at 70 °C (c-NiHCF-70°C), and the synthesis of r-NiHCF was performed at 90 °C (r-NiHCF-90°C). These temperatures were chosen to produce c-NiHCF and r-NiHCF with morphologies and crystallinities that were as similar as possible so that the only difference between these two samples was the lattice-type. SEM images show that both c-NiHCF-70°C (Figure 3c) and r-NiHCF-90°C (Figure 3d) are composed of

Table 1. Chemical Formulas of Each NiHCF Sample Determined by Elemental Analysis (EDS) and Water Content Measured as Percent Mass Loss Using TGA

	chemical formula	Fe(CN) ₆ vacancies (%)	water content (%)
c-NiHCF-RT	$K_{0.05}Na_{0.07}Ni[Fe(CN)_6]_{0.65} \cdot nH_2O$	35	19.1
r-NiHCF-RT	$Na_{1.20}Ni[Fe(CN)_6]_{0.85} \cdot nH_2O$	15	9.8
c-NiHCF-70°C	$K_{0.31}Na_{0.33}Ni[Fe(CN)_6]_{0.80}\cdot nH_2O$	20	16.3
r-NiHCF-90°C	$Na_{1.55}Ni[Fe(CN)_6]_{0.93} \cdot nH_2O$	7	8.4

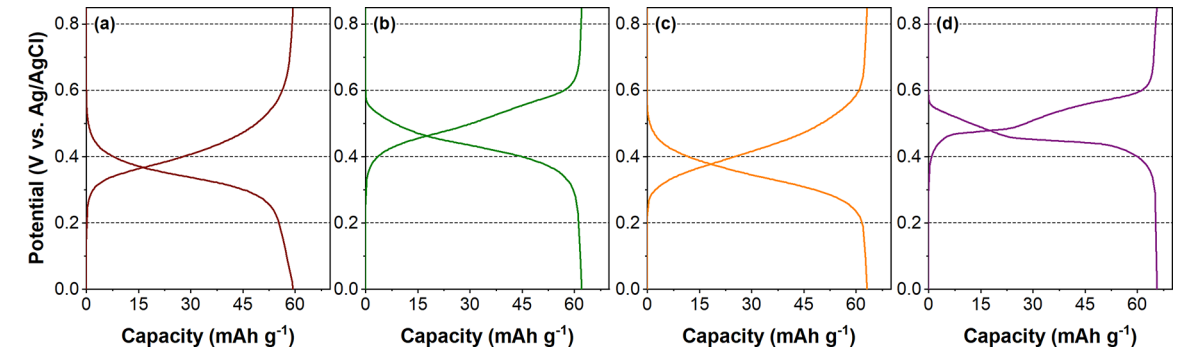


Figure 5. Potential—capacity plots of (a) c-NiHCF-RT, (b) r-NiHCF-RT, (c) c-NiHCF-70°C, and (d) r-NiHCF-90°C. All measurements were obtained in 0.6 M NaCl at a rate of ~2.5C with cutoff potentials of 0 and 0.85 V vs Ag/AgCl for sodiation and desodiation, respectively.

large, micrometer-sized cubes and the cubes are similar in size. The formation of the cubic and rhombohedral phases was again confirmed by XRD. All peaks of c-NiHCF-70°C can be assigned to the cubic structure (Figure 4c), and r-NiHCF-90°C exhibits the characteristic peak splitting of the rhombohedral structure (Figure 4d). Judging from the FWHM of the (200) peaks, the two samples have similar crystallinities, although r-NiHCF-90°C (Figure 4d, left panel) is slightly more crystalline than c-NiHCF-70°C (Figure 4c, left panel), possibly because of the higher synthesis temperature used for r-NiHCF-90°C. Both c-NiHCF-70°C and r-NiHCF-90°C are much more crystalline than c-NiHCF-RT and r-NiHCF-RT.

The composition of all samples was evaluated by EDS and TGA to determine their chemical formulas and water content, and the results are summarized in Table 1. EDS was used to calculate the Fe:Ni ratio and determine the number of Fe(CN)₆ vacancies. Ideally, the Fe:Ni ratio should be 1:1 in a sample that contains no Fe(CN)₆ vacancies. TGA was used to evaluate the water content present within the crystal structure of each sample. Water molecules can occupy both the Fe(CN)₆ vacancy sites and empty A-sites. ^{29,30,43} The presence of K⁺ in the c-NiHCF samples is due to the use of K₃Fe(CN)₆ as the Fe^{III} precursor. We mentioned earlier that the latticetype of the as-prepared samples is governed by the oxidation state of Fe, which is coupled with the A-site occupancy of the structure. Indeed, the A-site occupancies (the sum of Na⁺ and K⁺) of the cubic samples (0.12 for c-NiHCF-RT and 0.64 for c-NiHCF-70°C) are much lower than those of the rhombohedral samples (1.20 for r-NiHCF-RT and 1.55 for r-NiHCF-90°C). On the basis of their chemical formulas, it is also clear that the cubic samples contain more Fe^{III} than the rhombohedral samples.

Table 1 shows that the high temperature samples contain fewer $Fe(CN)_6$ vacancies than the corresponding room temperature samples. This is because the use of a high temperature during the synthesis decreases the rate of precipitation of NiHCF crystals, enabling the slow growth of crystals with a low number of $Fe(CN)_6$ vacancies and high

crystallinity. Table 1 also shows that the rhombohedral samples generally contain fewer Fe(CN)₆ vacancies than the cubic samples. This is because the more regular A-site occupancy of the rhombohedral samples facilitates the growth of NiHCF crystals with fewer Fe(CN)₆ vacancies. 44 The combined effects of synthesis temperature and A-site occupancy can be used to explain why c-NiHCF-RT has the highest number of Fe(CN)₆ vacancies while r-NiHCF-90°C has the lowest number of Fe(CN)₆ vacancies. The r-NiHCF-RT and c-NiHCF-70°C samples contain a comparable number of Fe(CN)₆ vacancies. The water content of each sample is affected by both the number of Fe(CN)₆ vacancies and the A-site occupancy. Thus, in general the cubic NiHCF samples that contain a higher number of Fe(CN)₆ vacancies and have a lower A-site occupancy also have a higher water content than the rhombohedral NiHCF samples.

Lastly, the A-site occupancy of the as-prepared samples appears to be the major factor that governs the cell parameters. On the basis of the (h00) peak positions shown in Figure 4, d_{100} spacings of the four NiHCF samples were determined in the order of c-NiHCF-RT (10.24 Å) < c-NiHCF-70°C (10.28 Å) < r-NiHCF-RT (10.32 Å) < r-NiHCF-90°C (10.34 Å). This indicates that the rhombohedral samples prepared with higher A-site occupancies have larger d_{100} spacings than the cubic samples. Additionally, comparing samples with the same lattice-type reveals that the sample prepared at a higher temperature has a larger unit cell because high temperature samples commonly have a higher A-site occupancy.

Combined, characterization of the NiHCF samples confirms the fabrication of two sets of c-NiHCF and r-NiHCF samples with different particle sizes, morphologies, crystallinities, and lattice-types. The amount of ${\rm Fe^{II}}$ and ${\rm Na^+}$ present in the asprepared samples was shown to affect the lattice-type, lattice parameters, number of ${\rm Fe(CN)_6}$ vacancies, and water content. The synthesis temperature was shown to affect the particle size, crystallinity, and number of ${\rm Fe(CN)_6}$ vacancies. In the sections that follow, the effect of these structural and compositional features on the electrochemistry, sodiation/desodiation per-

formances, and structural transitions of each NiHCF sample will be examined.

Sodiation/Desodiation Performances and Structural Changes of c-NiHCF and r-NiHCF. To investigate the electrochemical performance of NiHCF for seawater desalination applications, the sodiation and desodiation performances of each sample were investigated in 0.6 M NaCl solutions to mimic the salinity of seawater. Potential-capacity plots were obtained at a current density of 145 mA g⁻¹ (~2.5C rate) and are presented in Figure 5. Cutoff potentials of 0 and 0.85 V vs Ag/AgCl were used for sodiation and desodiation, respectively. The potential—capacity plot of c-NiHCF-RT illustrates that it has a capacity of \sim 59 mAh g⁻¹ (Figure 5a), consistent with the capacity that is typically reported for NiHCF. The r-NiHCF-RT sample shows a slightly higher capacity of ~62 mAh g⁻¹ (Figure 5b), likely due the lower number of Fe(CN)₆ vacancies present in r-NiHCF-RT compared with c-NiHCF-RT. The c-NiHCF-70°C sample shows a capacity of ~62 mAh g⁻¹ (Figure 5c), and the r-NiHCF-90°C sample shows the highest capacity of \sim 65 mAh g⁻¹ (Figure 5d). The observed differences in capacity correlate well with the number of Fe(CN)₆ vacancies present in each NiHCF sample. 34,35,41 For example, r-NiHCF-RT and c-NiHCF-70°C have different lattice-types, morphologies, and crystallinities but have a comparable number of Fe(CN)6 vacancies and show comparable capacities.

In addition to variations in the capacity of each sample, the potential—capacity plots in Figure 5 call attention to two other notable differences. The first is related to the sodiation/desodiation potentials. The sodiation/desodiation potentials of the cubic NiHCF samples are commonly less positive than those of the rhombohedral NiHCF samples. The lattice-type-dependent sodiation/desodiation potential of NiHCF has also been observed in previous studies. 34,35,41 The second is related to the shape of the potential profiles. While c-NiHCF-RT and c-NiHCF-70°C exhibit only a single gradually sloping plateau during sodiation/desodiation (Figure 5a,c), r-NiHCF-90°C shows a clear slope change at ~0.45 V vs Ag/AgCl (Figure 5d).

These differences became clearer when the sodiation/ desodiation reactions of the cubic and rhombohedral samples were examined using cyclic voltammetry (CV) (Figure 6). The cathodic peaks shown in the CVs are due to the reduction of Fe^{III} to Fe^{II} coupled with the insertion of Na⁺ into the NiHCF structure (sodiation), and the anodic peaks are due to the oxidation of Fe^{II} to Fe^{III} coupled with the release of Na⁺ from the NiHCF structure (desodiation). In these CVs, c-NiHCF-RT and c-NiHCF-70°C clearly exhibit only one reduction/ oxidation peak, consistent with the shape of the voltage profiles shown in Figure 5a,c. However, r-NiHCF-90°C shows two distinct reduction/oxidation peaks, consistent with the slope change of the voltage profile shown in Figure 5d. Although it was not obvious in the potential-capacity plot of r-NiHCF-RT (Figure 5b), the CV of r-NiHCF-RT (Figure 6a) also shows two distinct reduction/oxidation peaks, suggesting that the existence of two reduction/oxidation peaks is a common feature of NiHCF samples prepared with rhombohedral latticetypes. The CVs also confirm that the two cubic samples have cathodic/anodic peaks that appear at less positive potentials than those of the two rhombohedral samples, which agrees well with the potential-capacity plots.

To investigate how the lattice-type of the as-prepared samples affects the electrochemistry and sodiation/desodiation

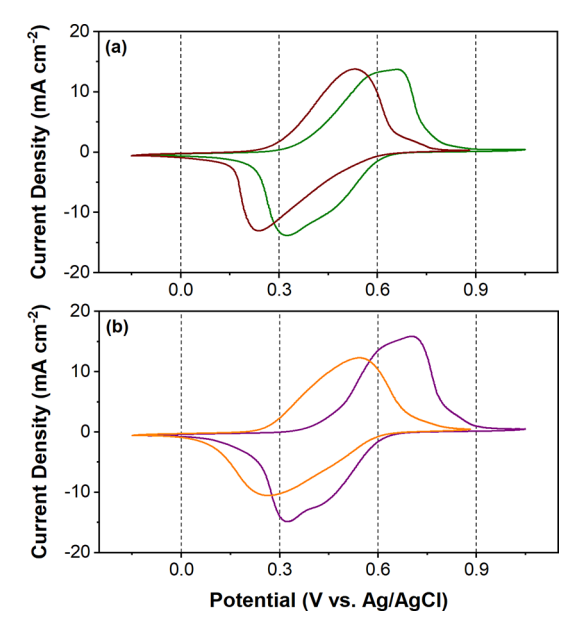


Figure 6. Cyclic voltammograms (CVs) of (a) c-NiHCF-RT (brown) and r-NiHCF-RT (green) and (b) c-NiHCF-70 $^{\circ}$ C (orange) and r-NiHCF-90 $^{\circ}$ C (purple). All CVs were obtained in 0.6 M NaCl with a scan rate of 2 mV s $^{-1}$.

processes of cubic and rhombohedral NiHCF, we used ex situ XRD measurements to examine the structural changes of NiHCF that occur during sodiation/desodiation. Figure 7

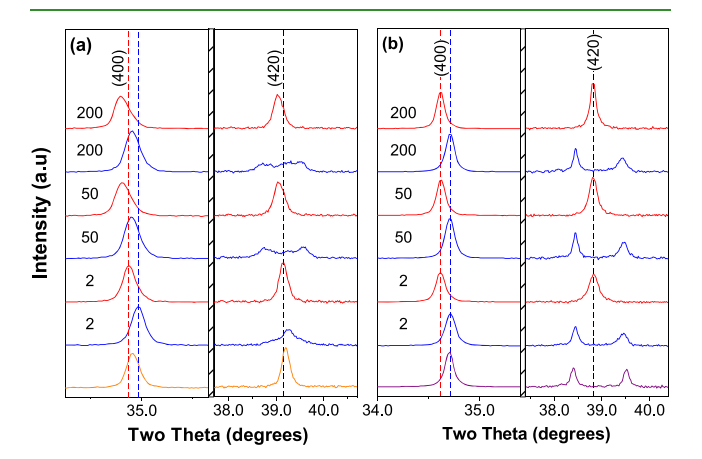


Figure 7. XRD patterns obtained after sodiation (blue lines) and desodiation (red lines) for (a) c-NiHCF-70°C and (b) r-NiHCF-90°C. The as-prepared electrodes are also shown as (a) the orange line and (b) the purple line. For clarity, only the (400) and (420) peaks are shown here and the (420) peaks have been magnified. The dashed blue lines are used to show the (400) peak position of the sodiated electrodes, the dashed red lines are used to show the (400) peak position of the desodiated electrodes, and the dashed black lines are used to show the (420) peak position.

shows the XRD patterns of sodiated (blue) and desodiated (red) c-NiHCF-70°C and r-NiHCF-90°C over the course of 200 cycles. The XRD patterns of the as-prepared electrodes are also shown. For clarity, only the (400) peaks and (420) peaks of selected cycles are shown in Figure 7. (Figure S1 shows XRD patterns over a wider range of 2θ values and for additional sodiation/desodiation cycles.) The XRD patterns of the high temperature samples are discussed in detail because they have more well-defined XRD peaks that enable us to more

clearly see subtle differences in the XRD patterns. The XRD patterns of the room temperature samples are shown in Figures S2 and S3 and show the same trends (Table S1) as those of the high temperature samples discussed below.

Figure 7 shows that when fully desodiated (red), both c-NiHCF-70°C and r-NiHCF-90°C possess cubic lattices as evidenced by the appearance of only a single peak at the (420) peak position. When fully sodiated, both samples possess rhombohedral lattices as evidenced by the appearance of doublets at the (420) peak position. The change in cell volume before and after sodiation can be estimated by comparing the positions of the (400) peaks, as the (400) peaks do not exhibit peak splitting during the structural transition. Figure 7 shows that the (400) peaks of both c-NiHCF-70°C and r-NiHCF-90°C commonly shifted to slightly higher 2θ values when sodiated, indicating a contraction of the unit cell. This means that an increase in the A-site occupancy during sodiation caused a contraction of the unit cell, although a higher A-site occupancy in the as-prepared samples resulted in the formation of a structure with a larger unit cell. A contraction of the unit cell after sodiation is counterintuitive but this behavior is consistently observed for NiHCF and other PBAs, such as CuHCF. 29,33,42,45-47 When PBAs contain sufficiently large interstitial sites that can accommodate Na+ without further cell expansion, it is possible that other electronic effects resulting from the change in oxidation state of Fe can be the dominant factor that causes a cell contraction upon sodiation. One previously reported plausible explanation for this behavior involves a change in the $-Fe-C-N-M-\pi$ orbital system; the reduction of Fe^{III} $(t_{2g}^{\ 5}e_g^{\ 0})$ to Fe^{II} $(t_{2g}^{\ 6}e_g^{\ 0})$ that occurs during sodiation can strengthen the π back-bonding and shorten the overall length of the -Fe-C-N-M- framework. 44,47 However, computational studies specifically on NiHCF would be necessary to verify this explanation.

The fact that these two samples are both cubic when desodiated and rhombohedral when sodiated regardless of the lattice-type of the as-prepared samples suggested that the lattice-type of the as-prepared samples, which is not maintained during sodiation/desodiation, cannot directly cause the electrochemical differences shown in Figures 5 and 6. (All experiments shown in Figures 5 and 6 were initiated with fully desodiated NiHCF electrodes that possessed cubic lattices.) Thus, there must be other structural differences between the samples that are related to the lattice-type of the as-prepared samples but can directly account for the observed differences in electrochemical behavior.

We note that although c-NiHCF-70°C and r-NiHCF-90°C commonly possess cubic lattices when desodiated and rhombohedral lattices when sodiated, the unit cell size of the two samples is not the same; c-NiHCF-70°C always has a smaller unit cell than r-NiHCF-90°C (Table 2). Thus, we believe that it is most likely the size of the unit cell and, therefore, the bond lengths within the -Fe-C-N-Ni-framework rather than the lattice-type itself that are directly responsible for the observed electrochemical differences. The lattice-type of the as-prepared sample appeared to be responsible only because it is linked to the size of the NiHCF unit cell.

With this understanding, the results shown in Figures 5 and 6 can be explained in terms of the different unit cell sizes of the different NiHCF samples. Figures 5 and 6 showed that the redox peaks of Fe^{II}/Fe^{III} (or sodiation/desodiation potentials) of the cubic NiHCF samples with smaller unit cell sizes

Table 2. Lattice Parameters of As-Prepared, Desodiated, and Sodiated c-NiHCF-70°C and r-NiHCF-90°C^a

	2θ (400)	d_{100}
as-prepared c-NiHCF-70°C	34.90	10.28
desodiated c-NiHCF-70°C	34.87	10.29
sodiated c-NiHCF-70°C	34.96	10.27
as-prepared r-NiHCF-90°C	34.71	10.34
desodiated r-NiHCF-90°C	34.62	10.37
sodiated r-NiHCF-90°C	34.74	10.33

^aThe lattice parameters of the sodiated and desodiated electrodes were calculated from the XRD patterns taken after the second sodiation and desodiation cycle.

occurred at less positive potentials than those of the rhombohedral NiHCF samples. (When the redox peaks appear at less positive potentials, the oxidation reaction is easier while the reduction reaction is more difficult.) Thus, these results imply that when the unit cell is smaller, the reduction of Fe^{III} to Fe^{II} coupled with the insertion of Na^+ into NiHCF is more difficult, and the oxidation of Fe^{II} to Fe^{III} coupled with the release of Na^+ from NiHCF is easier.

Another notable feature depicted in Figure 7a is that the (400) peak of both desodiated (cubic phase, red lines) and sodiated (rhombohedral phase, blue lines) c-NiHCF-70°C continues to shift to lower 2θ values after subsequent sodiation/desodiation cycles, indicating an expansion of the unit cell. We also note that the sodiated electrodes exhibit inconsistent peak splitting of the doublet that appears at the (420) position. This indicates that, after sodiation, the structure of c-NiHCF-70°C with a rhombohedral lattice is poorly crystalline and appears to be changing throughout the cycling test. This suggests that the unit cell of the as-prepared c-NiHCF-70°C sample may be too small, and it gradually increases during continued sodiation/desodiation cycles. In contrast, Figure 7b shows that the (400) peak of r-NiHCF-90°C after desodiation (cubic phase, red lines) appears in an identical position after subsequent sodiation/desodiation cycles. The same behavior is also observed for the (400) and (420) peaks of the sodiated electrodes (rhombohedral phase, blue lines). This indicates that the structural transition that occurs for r-NiHCF-90°C is stable and consistent. The sufficiently large cell size of the as-prepared r-NiHCF-90°C sample may be a possible reason for the observed behavior.

The results shown in Figure 7 provide new insights into how the unit cell size, which is governed by the lattice-type of the as-prepared sample, is directly responsible for the different electrochemical behavior of the cubic and rhombohedral NiHCF samples. However, the results shown in Figure 7 cannot explain why rhombohedral NiHCF samples show two redox peaks while cubic NiHCF samples show only one

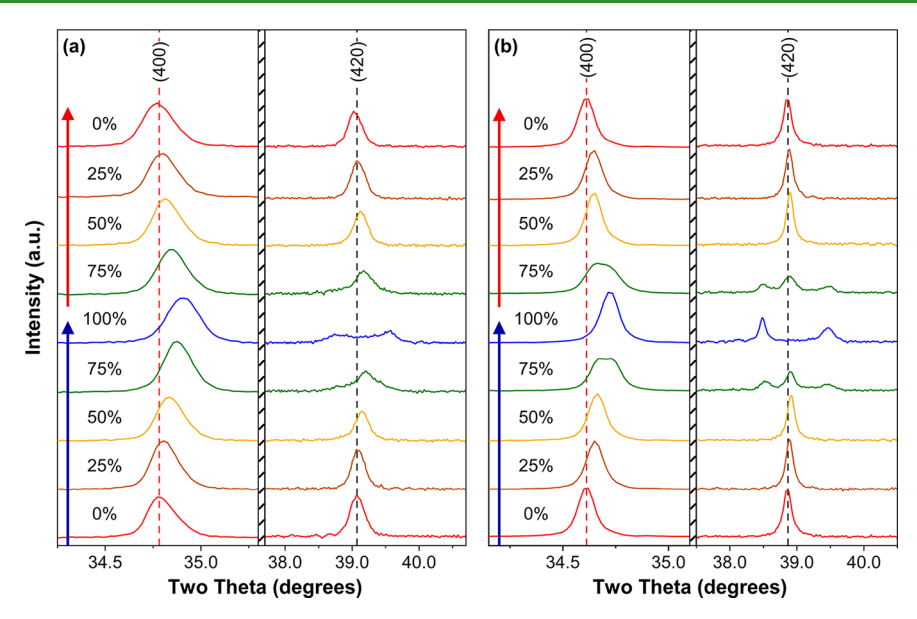


Figure 8. XRD patterns obtained at different degrees of sodiation for (a) c-NiHCF-70°C and (b) r-NiHCF-90°C. Each XRD pattern is labeled with the degree of sodiation as percent sodiation. The blue arrow indicates the direction of the sodiation reaction, and the red arrow indicates the direction of the desodiation reaction. For clarity, only the (400) and (420) peaks are shown here and the (420) peaks have been magnified. The dashed red lines are used to show the (400) peak position of the desodiated electrodes, and the dashed black lines are used to show the (420) peak position.

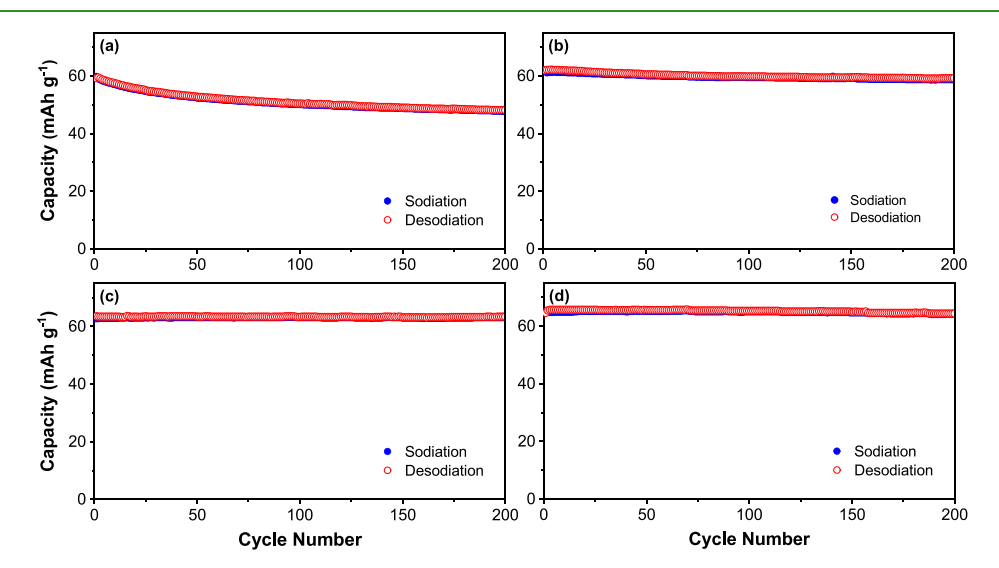


Figure 9. Cyclability of (a) c-NiHCF-RT, (b) r-NiHCF-RT, (c) c-NiHCF-70 $^{\circ}$ C, and (d) r-NiHCF-90 $^{\circ}$ C. All cycling tests were performed in 0.6 M NaCl at a rate of \sim 2.5C with cutoff potentials of 0 and 0.85 V vs Ag/AgCl for sodiation and desodiation, respectively.

(Figure 6). To elucidate the cause of this behavior, we took a closer look at the structural transition that occurs within each sodiation/desodiation step. Figure 8 shows ex situ XRD patterns obtained during the 200th cycle at different degrees of sodiation/desodiation. (XRD patterns taken over a wider range of 2θ values can be found in Figure S4.) The degree of sodiation is referred to as 0% when NiHCF is fully oxidized (100% Fe^{III}) and 100% when it is fully reduced (100% Fe^{III}).

Figure 8 shows that while c-NiHCF-70°C and r-NiHCF-90°C both exhibit a transition between rhombohedral and cubic phases after sodiation and desodiation, respectively, the degree of sodiation/desodiation that induces the structural transition is different for the two samples. For the c-NiHCF-70°C sample, the conversion from cubic to rhombohedral was observed only after 100% sodiation (Figure 8a). This means that throughout the sodiation reaction, cubic NiHCF existed as

a single cubic phase. For the reverse desodiation process, the structural transition from rhombohedral to cubic occurred as soon as the desodiation reaction was initiated. This means that throughout the desodiation reaction, cubic NiHCF also existed as a single cubic phase. These results explain why the voltage profiles of cubic NiHCF samples show a single uniform, gradually sloping plateau during sodiation/desodiation (Figure 5a.c.).

Examining the XRD patterns of r-NiHCF-90°C reveals different behavior. During sodiation of r-NiHCF-90°C, a single cubic phase exists only until 50% sodiation; at 75% sodiation the cubic and rhombohedral phases coexist (Figure 8b). This suggests that the initial sodiation reaction was performed while NiHCF had a cubic structure but the latter part of the sodiation reaction was performed after NiHCF was partially or fully converted to the rhombohedral structure. Upon

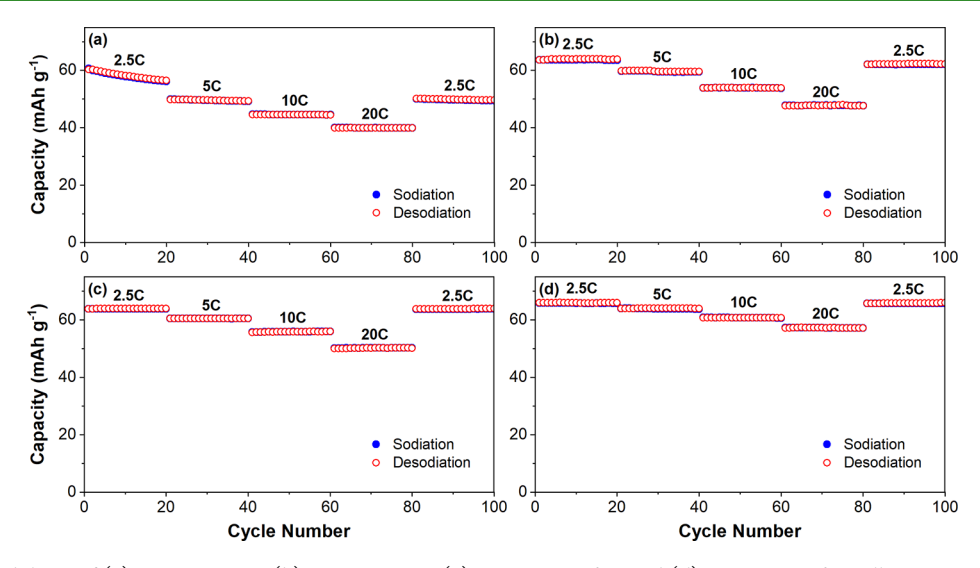


Figure 10. Rate capabilities of (a) c-NiHCF-RT, (b) r-NiHCF-RT, (c) c-NiHCF-70°C, and (d) r-NiHCF-90°C. All tests were performed in 0.6 M NaCl at current densities of 145 mA g^{-1} (\sim 2.5C), 290 mA g^{-1} (\sim 5C), 580 mA g^{-1} (\sim 10C), and 1160 mA g^{-1} (\sim 20C) with cutoff potentials of 0 and 0.85 V vs Ag/AgCl for sodiation and desodiation, respectively.

desodiation, the same structural transition was observed; the initial desodiation reaction was performed while the rhombohedral phase remained as a single phase or coexisted with the cubic phase, but the latter part of desodiation was performed while only the cubic phase existed. The presence of two phases during the sodiation/desodiation reaction explains why r-NiHCF-90°C shows a change in slope in the potential profiles presented in Figure 5d. The fact that r-NiHCF-90°C exhibits a cubic-to-rhombohedral transition at a lesser degree of sodiation may also be related to the larger unit cell size of r-NiHCF-90°C; in a larger cell, Na⁺ may have more freedom to reside at a position that is slightly displaced from the body center of the cube, more readily lowering the symmetry of the cell from cubic to rhombohedral.

Overall, the ex situ XRD results shown in Figures 7 and 8 provide critical information to better understand the relationship between the lattice-type and unit cell sizes of the asprepared, sodiated, and desodiated samples and the electrochemical properties and structural transitions that occur in NiHCF.

Evaluation of Cyclability and Rate Capabilities. The cyclability of each NiHCF sample was evaluated in 0.6 M NaCl at a current density of 145 mA $\rm g^{-1}$ (~2.5C). The voltage profiles obtained throughout the cycling tests can be found in Figure S5. Over the course of 200 cycles, the capacity of c-NiHCF-RT decreased from an initial value of 59 mAh $\rm g^{-1}$ to 48 mAh $\rm g^{-1}$, corresponding to a capacity retention of 83% (Figure 9a). The capacity of r-NiHCF-RT, on the other hand, only decreased from an initial value of 62 mAh $\rm g^{-1}$ to 59 mAh $\rm g^{-1}$, corresponding to a capacity retention of 95% (Figure 9b). The c-NiHCF-70°C and r-NiHCF-90°C samples both exhibited close to 100% capacity retention (Figure 9c,d).

As c-NiHCF-RT and r-NiHCF-RT both had relatively low crystallinity, these results show that the larger unit cell size of r-NiHCF-RT that undergoes more consistent structural transitions is advantageous for achieving better cyclability when a low-quality sample is used. However, the samples prepared at an elevated temperature with high crystallinity can achieve excellent cyclability regardless of the lattice-type of the as-prepared samples. In fact, to the best of our knowledge, the capacity retention shown here for c-NiHCF-70°C and r-

NiHCF-90°C is the highest reported to date for any PBA tested in aqueous solutions containing Cl⁻. These results are encouraging and illustrate that when properly optimized, NiHCF may in fact be stable in neutral saline solutions and can be used for practical seawater desalination.

Next, the rate capabilities of each sample were investigated by changing the current density from 145 mA g^{-1} (~2.5C) to 290 mA g^{-1} (~5C), 580 mA g^{-1} (~10C), 1160 mA g^{-1} (~20C), and back to 145 mA g^{-1} (~2.5C) in the same 0.6 M NaCl solution. These tests reveal that c-NiHCF-RT showed some capacity fading at the initial 2.5C rate and maintained only 67% of its initial capacity when the rate was increased to 20C (Figure 10a). Additionally, it recovered only 83% of its initial capacity when the rate was decreased back to 2.5C, demonstrating poor stability and rate capabilities. The r-NiHCF-RT sample, on the other hand, maintained 75% of its initial capacity when the rate was increased from 2.5C to 20C and recovered 98% of its initial capacity when the rate was decreased back to 2.5C (Figure 10b). The c-NiHCF-70°C sample was able to maintain 78% of its initial capacity at a rate of 20C and recovered 100% of its initial capacity when the rate was decreased back to 2.5C (Figure 10c). It is interesting to note that the rate capabilities of r-NiHCF-RT and c-NiHCF-70°C are comparable although they differ in terms of latticetype, unit cell size, particle size, morphology, and crystallinity. However, the one structural feature that they share is a comparable number of Fe(CN)₆ vacancies. The primary advantage of c-NiHCF-70°C is its high crystallinity, while the primary advantage of r-NiHCF-RT is the consistent structural changes that occur during cycling. Thus, it is possible that the advantages offered by each sample are equivalent and result in comparable rate capabilities. As expected, the r-NiHCF-90°C sample, which is the most crystalline, has the fewest number of Fe(CN)6 vacancies, and shows consistent structural changes during cycling, demonstrates the best rate capabilities; it maintained 87% of its initial capacity when the rate was increased from 2.5C to 20C and recovered close to 100% of its initial capacity when the rate was decreased back to 2.5C (Figure 10d).

Another important characteristic of Na-storage electrodes that should be examined is the reversibility of the sodiation/

desodiation reaction, which can be evaluated by the voltage hysteresis (the difference between the sodiation and desodiation potential profiles). The voltage hysteresis of each NiHCF sample at a rate of 2.5C is shown in Figure S6. For clarity, all desodiation potential profiles were inverted. To illustrate trends based on the voltage hysteresis, we examined the difference in average sodiation and desodiation potentials for each NiHCF sample. These values are 0.049 V for c-NiHCF-RT, 0.041 V for r-NiHCF-RT, 0.045 V for c-NiHCF-70°C, and 0.038 V for r-NiHCF-90°C. The difference in voltage required for the sodiation and desodiation reactions directly affects the energy efficiency of conventional batteries and desalination batteries (energy output generated during discharging/energy input required for charging). Therefore, r-NiHCF-90°C will be able to achieve the highest energy efficiency among the samples prepared here. This means that in terms of capacity, cyclability, rate capabilities, and energy efficiency, r-NiHCF-90°C is the most promising candidate for desalination and energy storage applications. Overall, the results presented in this work suggest that preparing PBAs under slow crystal growth conditions with a high A-site occupancy, a minimum number of Fe(CN)6 vacancies, and high crystallinity is the key to constructing efficient and stable PBA electrodes.

4. CONCLUSION

In summary, we successfully synthesized two sets of cubic and rhombohedral NiHCF samples with different particle sizes, crystallinities, and compositions. We showed that the amount of Fe^{II} and A-site occupancy of the as-prepared samples affects the lattice-type, lattice parameters, number of Fe(CN)₆ vacancies, and water content. The synthesis temperature was shown to affect the particle size, crystallinity, and number of Fe(CN)₆ vacancies. Potential-capacity plots and CVs revealed that the sodiation/desodiation reaction of rhombohedral NiHCF samples commonly occurred at more positive potentials than cubic NiHCF samples. The rhombohedral NiHCF samples also showed two redox peaks, while the cubic NiHCF samples showed only one redox peak during sodiation/desodiation. Ex situ XRD studies were used to establish that all samples have cubic lattices when desodiated and rhombohedral lattices when sodiated. This suggested that the lattice-type of the as-prepared samples cannot be the direct cause of the observed differences in electrochemical behavior because the original lattice-type is not maintained during sodiation/desodiation. Careful analysis of ex situ XRD patterns indicated that the lattice size of the as-prepared samples is likely the direct cause for the different electrochemical behavior of the different samples. The two redox peaks present for the rhombohedral samples were attributed to a cubic-torhombohedral transition that occurs in the middle of the sodiation/desodiation process. The cubic samples, on the other hand, only exhibited a cubic-to-rhombohedral transition upon completion of sodiation or initiation of desodiation. The ex situ XRD studies also revealed that the lattice size of cubic NiHCF samples continuously expanded during subsequent sodiation/desodiation cycles while that of rhombohedral NiHCF samples remained the same.

Our study also confirmed that the capacity of each sample was determined by the number of Fe(CN)₆ vacancies present in the sample. The capacity retention during the cycling test was primarily affected by the crystallinity, and both c-NiHCF-70°C and r-NiHCF-90°C with high crystallinity exhibited close

to 100% capacity retention for 200 cycles in 0.6 M NaCl. This is the highest capacity retention of any PBA reported to date in neutral aqueous electrolytes containing Cl-. These results are encouraging and illustrate that when properly optimized, NiHCF may in fact be used for practical seawater desalination. Additionally, r-NiHCF-90°C, which is the most crystalline, has the fewest number of Fe(CN)₆ vacancies and shows consistent structural changes during cycling, demonstrated exceptional rate capabilities, and was able to retain 87% of its initial capacity when the rate was increased from 2.5C to 20C. Furthermore, r-NiHCF-90°C showed a minimal voltage hysteresis that will result in high energy efficiency when it is used as a Na-storage electrode in the desalination cell architectures shown in Figure 1. These features make the r-NiHCF-90°C sample reported in this study a promising candidate for further practical investigations. The new understanding and insights provided in this study regarding the structure-performance relationships of NiHCF will help to facilitate the construction of more efficient and stable NiHCF and other PBA electrodes for desalination and energy storage applications.

ASSOCIATED CONTENT

5 Supporting Information

The Supporting Information is available free of charge at https://pubs.acs.org/doi/10.1021/acsami.0c08084.

Additional XRD results, lattice parameters of room temperature samples, voltage profiles during cycling tests, and voltage hysteresis plots (PDF)

AUTHOR INFORMATION

Corresponding Author

Kyoung-Shin Choi — Department of Chemistry, University of Wisconsin—Madison, Madison, Wisconsin 53706, United States; orcid.org/0000-0003-1945-8794; Email: kschoi@chem.wisc.edu

Authors

Margaret A. Lumley – Department of Chemistry, University of Wisconsin—Madison, Madison, Wisconsin 53706, United

Do-Hwan Nam – Department of Chemistry, University of Wisconsin—Madison, Madison, Wisconsin 53706, United States; orcid.org/0000-0002-5601-3172

Complete contact information is available at: https://pubs.acs.org/10.1021/acsami.0c08084

Notes

The authors declare no competing financial interest.

ACKNOWLEDGMENTS

This work was supported by the Draper Technology Innovation Fund (University of Wisconsin-Madison) and the National Science Foundation (NSF) through Grant CBET-1803496.

REFERENCES

- (1) Runte, G. Seawater and Brackish Water Desalination; MST052D; BCC Research; Wellesley, MA, 2016.
- (2) Gude, V. G.; Nirmalakhandan, N.; Deng, S. Renewable and Sustainable Approaches for Desalination. *Renewable Sustainable Energy Rev.* **2010**, *14*, 2641–2654.

- (3) Elimelech, M.; Phillip, W. A. The Future of Seawater Desalination: Energy, Technology, and the Environment. *Science* **2011**, 333, 712–717.
- (4) Ghaffour, N.; Missimer, T. M.; Amy, G. L. Technical Review and Evaluation of the Economics of Water Desalination: Current and Future Challenges for Better Water Supply Sustainability. *Desalination* **2013**, *309*, 197–207.
- (5) Ghaffour, N.; Bundschuh, J.; Mahmoudi, H.; Goosen, M. F. A. Renewable Energy-Driven Desalination Technologies: A Comprehensive Review on Challenges and Potential Applications of Integrated Systems. *Desalination* **2015**, *356*, 94–114.
- (6) Burn, S.; Hoang, M.; Zarzo, D.; Olewniak, F.; Campos, E.; Bolto, B.; Barron, O. Desalination Techniques A Review of the Opportunities for Desalination in Agriculture. *Desalination* **2015**, 364. 2–16.
- (7) Pasta, M.; Wessells, C. D.; Cui, Y.; La Mantia, F. A Desalination Battery. *Nano Lett.* **2012**, *12*, 839–843.
- (8) Nam, D.-H.; Choi, K.-S. Bismuth as a New Chloride-Storage Electrode Enabling the Construction of a Practical High Capacity Desalination Battery. *J. Am. Chem. Soc.* **2017**, *139*, 11055–11063.
- (9) Chen, F.; Huang, Y.; Guo, L.; Sun, L.; Wang, Y.; Yang, H. Y. Dual-Ions Electrochemical Deionization: A Desalination Generator. *Energy Environ. Sci.* **2017**, *10*, 2081–2089.
- (10) Chen, F.; Huang, Y.; Guo, L.; Ding, M.; Yang, H. Y. A Dual-Ion Electrochemistry Deionization System Based on AgCl-Na_{0.44}MnO₂ Electrodes. *Nanoscale* **2017**, *9*, 10101–10108.
- (11) Chen, F.; Huang, Y.; Kong, D.; Ding, M.; Huang, S.; Yang, H. Y. NaTi₂(PO₄)₃-Ag Electrodes Based Desalination Battery and Energy Recovery. *FlatChem* **2018**, *8*, 9–16.
- (12) Srimuk, P.; Halim, J.; Lee, J.; Tao, Q.; Rosen, J.; Presser, V. Two-Dimensional Molybdenum Carbide (MXene) with Divacancy Ordering for Brackish and Sea Water Desalination via Cation and Anion Intercalation. ACS Sustainable Chem. Eng. 2018, 6, 3739–3747.
- (13) Nam, D.-H.; Lumley, M. A.; Choi, K.-S. A Desalination Battery Combining $Cu_3[Fe(CN)_6]_2$ as a Na-Storage Electrode and Bi as a Cl-Storage Electrode Enabling Membrane-Free Desalination. *Chem. Mater.* **2019**, *31*, 1460–1468.
- (14) Lee, J.; Kim, S.; Kim, C.; Yoon, J. Hybrid Capacitive Deionization to Enhance the Desalination Performance of Capacitive Techniques. *Energy Environ. Sci.* **2014**, *7*, 3683–3689.
- (15) Kim, S.; Lee, J.; Kim, C.; Yoon, J. Na₂FeP₂O₇ as a Novel Material for Hybrid Capacitive Deionization. *Electrochim. Acta* **2016**, 203, 265–271
- (16) Lee, J.; Kim, S.; Yoon, J. Rocking Chair Desalination Battery Based on Prussian Blue Electrodes. ACS Omega 2017, 2, 1653–1659.
- (17) Kim, T.; Gorski, C. A.; Logan, B. E. Low Energy Desalination Using Battery Electrode Deionization. *Environ. Sci. Technol. Lett.* **2017**, *4*, 444–449.
- (18) Porada, S.; Shrivastava, A.; Bukowska, P.; Biesheuvel, P. M.; Smith, K. C. Nickel Hexacyanoferrate Electrodes for Continuous Cation Intercalation Desalination of Brackish Water. *Electrochim. Acta* **2017**, 255, 369–378.
- (19) Guo, L.; Mo, R.; Shi, W.; Huang, Y.; Leong, Z. Y.; Ding, M.; Chen, F.; Yang, H. Y. A Prussian Blue Anode for High Performance Electrochemical Deionization Promoted by the Faradaic Mechanism. *Nanoscale* **2017**, *9*, 13305–13312.
- (20) Shrivastava, A.; Smith, K. C. Electron Conduction in Nanoparticle Agglomerates Limits Apparent Na⁺ Diffusion in Prussian Blue Analogue Porous Electrodes. *J. Electrochem. Soc.* **2018**, 165, 1777–1787.
- (21) Choi, S.; Chang, B.; Kim, S.; Lee, J.; Yoon, J.; Choi, J. W. Battery Electrode Materials with Omnivalent Cation Storage for Fast and Charge-Efficient Ion Removal of Asymmetric Capacitive Deionization. *Adv. Funct. Mater.* **2018**, 28, 1802665.
- (22) Suss, M. E.; Presser, V. Water Desalination with Energy Storage Electrode Materials. *Joule* **2018**, *2*, 10–15.
- (23) Yu, F.; Wang, L.; Wang, Y.; Shen, X.; Cheng, Y.; Ma, J. Faradaic Reactions in Capacitive Deionization for Desalination and Ion Separation. *J. Mater. Chem. A* **2019**, *7*, 15999.

- (24) Desai, D.; Beh, E. S.; Sahu, S.; Vedharathinam, V.; van Overmeere, Q.; de Lannoy, C. F.; Jose, A. P.; Völkel, A. R.; Rivest, J. B. Electrochemical Desalination of Seawater and Hypersaline Brines with Coupled Electricity Storage. *ACS Energy Lett.* **2018**, *3*, 375–379.
- (25) Nam, D.-H.; Choi, K.-S. Electrochemical Desalination Using Bi/BiOCl Electrodialysis Cells. ACS Sustainable Chem. Eng. 2018, 6, 15455–15462.
- (26) Nam, D.-H.; Choi, K.-S. Tandem Desalination/Salination Strategies Enabling the Use of Redox Couples for Efficient and Sustainable Electrochemical Desalination. *ACS Appl. Mater. Interfaces* **2019**, *11*, 38641–38647.
- (27) Kim, H.; Hong, J.; Park, K. Y.; Kim, H.; Kim, S. W.; Kang, K. Aqueous Rechargeable Li and Na Ion Batteries. *Chem. Rev.* **2014**, *114*, 11788–11827.
- (28) Wessells, C. D.; Peddada, S. V.; Huggins, R. A.; Cui, Y. Nickel Hexacyanoferrate Nanoparticle Electrodes For Aqueous Sodium and Potassium Ion Batteries. *Nano Lett.* **2011**, *11*, 5421–5425.
- (29) Ojwang, D. O.; Grins, J.; Wardecki, D.; Valvo, M.; Renman, V.; Häggström, L.; Ericsson, T.; Gustafsson, T.; Mahmoud, A.; Hermann, R. P.; Svensson, G. Structure Characterization and Properties of K-Containing Copper Hexacyanoferrate. *Inorg. Chem.* **2016**, *55*, 5924–5934.
- (30) Xu, Y.; Zheng, S.; Tang, H.; Guo, X.; Xue, H.; Pang, H. Prussian Blue and Its Derivatives as Electrode Materials for Electrochemical Energy Storage. *Energy Storage Materials.* **2017**, *9*, 11–30.
- (31) Li, W.; Han, C.; Cheng, G.; Chou, S.; Liu, H.; Dou, S. Chemical Properties, Structural Properties, and Energy Storage Applications of Prussian Blue Analogues. *Small* **2019**, *15*, 1900470.
- (32) Bauer, A.; Song, J.; Vail, S.; Pan, W.; Barker, J.; Lu, Y. The Scale-up and Commercialization of Nonaqueous Na-Ion Battery Technologies. *Adv. Energy Mater.* **2018**, *8*, 1702869.
- (33) Wessells, C. D.; Huggins, R. A.; Cui, Y. Copper Hexacyanoferrate Battery Electrodes with Long Cycle Life and High Power. *Nat. Commun.* **2011**, *2*, 550.
- (34) Xu, Y.; Wan, J.; Huang, L.; Ou, M.; Fan, C.; Wei, P.; Peng, J.; Liu, Y.; Qiu, Y.; Sun, X.; Fang, C.; Li, Q.; Han, J.; Huang, Y.; Alonso, J. A.; Zhao, Y. Structure Distortion Induced Monoclinic Nickel Hexacyanoferrate as High-Performance Cathode for Na-Ion Batteries. *Adv. Energy Mater.* **2019**, *9*, 1803158.
- (35) Xie, B.; Wang, L.; Shu, J.; Zhou, X.; Yu, Z.; Huo, H.; Ma, Y.; Cheng, X.; Yin, G.; Zuo, P. Understanding the Structural Evolution and Lattice Water Movement for Rhombohedral Nickel Hexacyanoferrate upon Sodium Migration. ACS Appl. Mater. Interfaces 2019, 11, 46705–46713.
- (36) Wu, X.; Sun, M.; Guo, S.; Qian, J.; Liu, Y.; Cao, Y.; Ai, X.; Yang, H. Vacancy-Free Prussian Blue Nanocrystals with High Capacity and Superior Cyclability for Aqueous Sodium-Ion Batteries. *ChemNanoMat* **2015**, *1*, 188–193.
- (37) Su, D.; McDonagh, A.; Qiao, S.-Z.; Wang, G. High-Capacity Aqueous Potassium-Ion Batteries for Large-Scale Energy Storage. *Adv. Mater.* **2017**, *29*, 1604007.
- (38) Paolella, A.; Faure, C.; Timoshevskii, V.; Marras, S.; Bertoni, G.; Guerfi, A.; Vijh, A.; Armand, M.; Zaghib, K. A Review on Hexacyanoferrate-Based Materials for Energy Storage and Smart Windows: Challenges and Perspectives. *J. Mater. Chem. A* **2017**, *5*, 18919–18932.
- (39) Huggins, R. A. Review-A New Class of High Rate, Long Cycle Life, Aqueous Electrolyte Battery Electrodes. *J. Electrochem. Soc.* **2017**, *164*, 5031–5036.
- (40) Shrivastava, A.; Liu, S.; Smith, K. C. Linking Capacity Loss and Retention of Nickel Hexacyanoferrate to a Two-Site Intercalation Mechanism for Aqueous Mg²⁺ and Ca²⁺ Ions. *Phys. Chem. Chem. Phys.* **2019**, *21*, 20177–20188.
- (41) Ji, Z.; Han, B.; Liang, H.; Zhou, C.; Gao, Q.; Xia, K.; Wu, J. On the Mechanism of the Improved Operation Voltage of Rhombohedral Nickel Hexacyanoferrate as Cathodes for Sodium-Ion Batteries. *ACS Appl. Mater. Interfaces* **2016**, *8*, 33619–33625.

- (42) Ren, W.; Qin, M.; Zhu, Z.; Yan, M.; Li, Q.; Zhang, L.; Liu, D.; Mai, L. Activation of Sodium Storage Sites in Prussian Blue Analogues via Surface Etching. *Nano Lett.* **2017**, *17*, 4713–4718.
- (43) Herren, F.; Fischer, P.; Ludi, A.; Halg, W. Neutron Diffraction Study of Prussian Blue, $Fe_4[Fe(CN)_6]_3$ *xH20. Location of Water Molecules and Long-Range Magnetic Order. *Inorg. Chem.* **1980**, *19*, 956–959.
- (44) Dostal, A.; Kauschka, G.; Reddy, S. J.; Scholz, F. Lattice Contractions and Expansions Accompanying the Electrochemical Conversions of Prussian Blue and the Reversible and Irreversible Insertion of Rubidium and Thallium Ions. *J. Electroanal. Chem.* **1996**, 406, 155–163.
- (45) Chae, M. S.; Heo, J. W.; Kwak, H. H.; Lee, H.; Hong, S. T. Organic Electrolyte-Based Rechargeable Zinc-Ion Batteries Using Potassium Nickel Hexacyanoferrate as a Cathode Material. *J. Power Sources* **2017**, 337, 204–211.
- (46) Hurlbutt, K.; Wheeler, S.; Capone, I.; Pasta, M. Prussian Blue Analogs as Battery Materials. *Joule* **2018**, *2*, 1950–1960.
- (47) Renman, V.; Ojwang, D. O.; Valvo, M.; Gómez, C. P.; Gustafsson, T.; Svensson, G. Structural-Electrochemical Relations in the Aqueous Copper Hexacyanoferrate-Zinc System Examined by Synchrotron X-ray Diffraction. J. Power Sources 2017, 369, 146–153.